

Electrocatalysis

Defect-Rich High-Entropy Oxide Nanosheets for Efficient 5-Hydroxymethylfurfural Electrooxidation

Kaizhi Gu⁺, Dongdong Wang⁺, Chao Xie, Tehua Wang, Gen Huang, Yanbo Liu, Yuqin Zou,^{*} Li Tao,^{*} and Shuangyin Wang^{*}

Abstract: High-entropy oxides (HEOs), a new concept of entropy stabilization, exhibit unique structures and fascinating properties, and are thus important class of materials with significant technological potential. However, the conventional high-temperature synthesis techniques tend to afford micron-scale HEOs with low surface area, and the catalytic activity of available HEOs is still far from satisfactory because of their limited exposed active sites and poor intrinsic activity. Here we report a low-temperature plasma strategy for preparing defect-rich HEOs nanosheets with high surface area, and for the first time employ them for 5-hydroxymethylfurfural (HMF) electrooxidation. Owing to the nanosheets structure, abundant oxygen vacancies, and high surface area, the quinary (FeCrCoNiCu)₃O₄ nanosheets deliver improved activity for HMF oxidation with lower onset potential and faster kinetics, outperforming that of HEOs prepared by high-temperature method. Our method opens new opportunities for synthesizing nanostructured HEOs with great potential applications.

Electrocatalytic conversion of biomass-derived molecules provides an attractive approach to obtain high value-added chemicals using renewable energy.^[1–4] For instance, the electrooxidation of 5-hydroxymethylfurfural (HMF) to 2,5-furandicarboxylic acid (FDCA) has drawn tremendous attention because FDCA is a promising alternative of petroleum-derived terephthalic acid for the production of biorenewable polymers. Furthermore, electrochemical oxidation of HMF is considered as a clean and environment-friendly route because this transformation is driven by electrons at the anode without the use of toxic chemical oxidants. In recent years, various metal-based electrocatalysts, such as sulfides, phosphides, and nitrides, have been explored for the HMF electrooxidation.^[5–9] Therefore, the development of robust, stable, and inexpensive electrocatalysts for efficient HMF oxidation to FDCA under mild conditions is highly desirable.

High-entropy materials (HEMs) are crystalline solid solutions that comprise five or more elements, in equimolar

or near-equimolar ratios, randomly distributed throughout a crystal structure.^[10–13] Based on the discovery of entropy-driven phase-stabilization effect, Rost et al. reported the first high-entropy oxides (HEOs) and expanded the library of HEMs.^[14] Afterwards, several kinds of HEOs with different crystal structures, such as rocksalt, spinel, perovskite, and fluorite, were exploited and technologically important in many applications, including electronics, catalysis, and energy storage and conversion.^[15–20] At present, the conventional synthetic routes toward HEOs are generally dominated by high-temperature approaches ($T \geq 900^\circ\text{C}$). However, these methods offer limited control over shape and size, and tend to form micron-scale materials with low surface area (Figure 1 a).^[20–24] The catalytic activity of HEOs is still far from satisfactory because of their limited exposed active sites and poor intrinsic activity.

Nanostructuring represents a promising strategy to enhance the activity of electrocatalysts, since nanostructured catalysts with high surface area can effectively increase the density of the exposed active sites and enhance mass diffusion efficiency, leading to improved electrocatalytic performance.^[25–28] However, one of the major obstacles encountered with the fabrication of nanostructured HEOs is the incompatible requirements of achieving high configurational entropy, which is driven by high-temperature processes, and preventing particle coarsening, which is facilitated by low-temperature reactions.^[29] In addition to expose more active surfaces, defect engineering such as introduction of oxygen vacancies is another effective strategy to promote the electrocatalytic activity.^[30–34] However, capabilities for the rational design and synthesis of nanostructured HEOs, especially two-dimensional (2D) HEOs nanosheets with oxygen vacancies under low temperature yet remain challenging.

Here, we report a low-temperature plasma strategy towards the synthesis of HEOs nanosheets with rich oxygen vacancies (Figure 1 b). Plasma is a promising technology for the synthesis and modification of nanomaterials.^[35,36] High-energy electrons collide inelastically with oxygen molecules and transfer their energy to the latter, which leads to the production of excited oxygen species with a significantly higher chemical activity than molecular oxygen. High-entropy layered double hydroxides (HE-LDHs)^[37] as precursors can be oxidized by high active oxygen species and converted into single-phase, spinel-type HEOs under mild conditions. Low-temperature plasma technique endows the as-synthesized HEOs with the nanosheets structure, abundant oxygen vacancies, and high surface area, which is beneficial for the improvement of the electrocatalytic active. As a proof

[*] Dr. K. Gu,^[†] D. Wang,^[†] Dr. C. Xie, Dr. T. Wang, G. Huang, Y. Liu, Y. Zou, Dr. L. Tao, Prof. Dr. S. Wang
 State Key Laboratory of Chemo/Bio-Sensing and Chemometrics,
 College of Chemistry and Chemical Engineering, Hunan University
 Changsha, 410082 (China)
 E-mail: yuqin_zou@hnu.edu.cn
 taoli@hnu.edu.cn
 shuangyinwang@hnu.edu.cn

[†] These authors contributed equally to this work.

 Supporting information and the ORCID identification number(s) for the author(s) of this article can be found under:
 <https://doi.org/10.1002/anie.202107390>

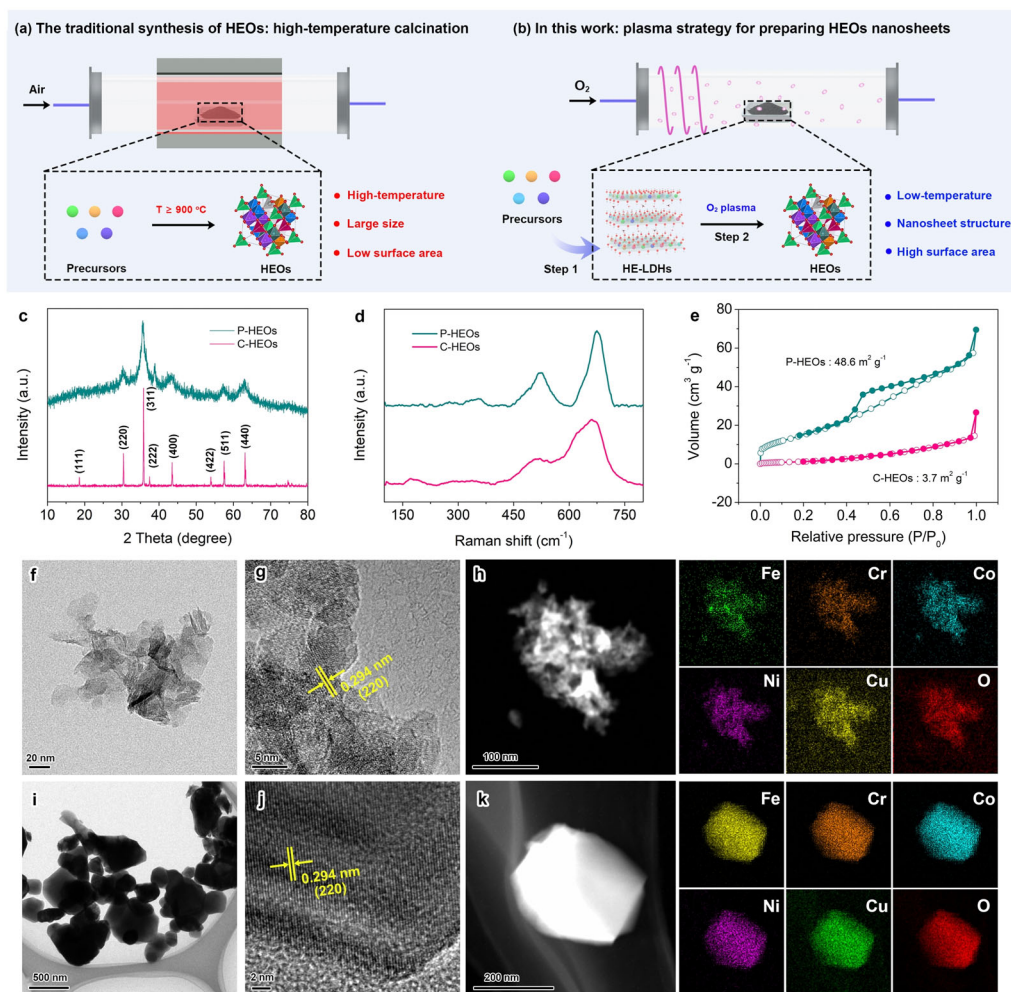


Figure 1. a) The traditional synthesis method and b) low-temperature plasma strategy for HEOs. c) XRD patterns, d) Raman spectra, and e) N_2 adsorption-desorption isotherm of P-HEOs and C-HEOs. f and i) TEM, g and j) HRTEM, and h and k) EDX mapping of P-HEOs and C-HEOs, respectively.

of concept, we use the representative quinary HEOs nanosheets as electrocatalysts for HMF electrooxidation. The $(\text{FeCrCoNiCu})_3\text{O}_4$ nanosheets exhibit superior electrocatalytic activity for HMF oxidation with lower onset potential and faster kinetics, providing a promising platform for efficient electrochemical HMF oxidation.

To demonstrate low-temperature plasma strategy, we first take quinary HEOs as an example for fabricating uniformly dispersed, single-phase, solid-solution nanosheets. Our method for the production of HEOs nanosheets follows a two-step process (Figure 1b). First, five metal salts (Fe, Cr, Co, Ni, and Cu) were mixed and formed HE-LDHs by the solvothermal method, which is a rational pathway for randomly assembling various metal atoms into 2D nanostructures.^[37] Then, we exposed the HE-LDHs to low-temperature oxygen plasma to form HEOs denoted as P-HEOs. For comparison, we also synthesized the control sample (C-HEOs) via reverse co-precipitation method at 1000 °C.^[24]

As shown in Figure 1c, XRD patterns of both P-HEOs and C-HEOs show eight major diffraction peaks corresponding to (111), (220), (311), (222), (400), (422), (511), and (440) planes of spinel phase structure ($Fd-3m$). Comparing with the

C-HEOs, we noticed that P-HEOs show a relatively decreased crystallinity due to the presence of structural defects. Meanwhile, the Raman spectrum of P-HEOs shows three features of E_g (350 cm^{-1}), F_{2g} (515 cm^{-1}), and A_{1g} (675 cm^{-1}) attributed to the characteristic vibrational modes of $Fd-3m$ space group (Figure 1d).^[22,38] It should be noted that the entropy-stabilized oxides contain Fe, Cr, Co, Ni, and Cu elements and their molar ratios are approximately 1: 1: 1: 1: 1, which is confirmed by energy dispersive X-ray (EDX) spectroscopy and inductively coupled plasma optical emission spectroscopy (ICP-OES) (Figure S1, Table S1 and S2). These results jointly validate that we have successfully synthesized spinel HEOs by the low-temperature plasma strategy. The formation of high-entropy phase is mainly driven by the high configurational entropy, which originates from the mixing of the multiple elements. The P-HEOs display a typical type-IV isotherm with a clear adsorption-desorption hysteresis loop, and the Brunauer-Emmett-Teller (BET) specific surface area of P-HEOs and C-HEOs are $48.6\text{ m}^2\text{ g}^{-1}$, respectively (Figure 1e). The high surface area of P-HEOs can expose of more active sites.^[39–41] The pore size distributions reveal that, compared with C-HEOs, the existence of more abundant

mesoporous structures in the P-HEOs (Figure S2), which facilitates the efficient mass transfer in biomass conversion.

The microstructure of HEOs was further evidenced by transmission electron microscopy (TEM). The TEM image shows the morphology of P-HEOs is nanosheets with size of ca. 20 nm (Figure 1 f). By contrast, the C-HEOs show the particle with diameter of about 500 nm because the cohesive energy drives codomain formation and sintering at 1000 °C (Figure 1 i). In contrast with the relatively smooth and compact surface of C-HEOs, P-HEOs nanosheets exhibit a rather rough and defective structure derived from the etching effect of plasma, which would promote electrocatalytic activity. The high-resolution TEM (HRTEM) images of P-HEOs and C-HEOs display lattice fringes with an interplanar distance of 0.294 nm correspond to the (220) planes of spinel (Figures 1 g and j), in line with the XRD results. The EDX mappings illustrate that Fe, Cr, Co, Ni, Cu, and O are all present and uniformly distributed, indicative of the formation of the high-entropy phase (Figures 1 h and k).

The X-ray photoelectron spectroscopy (XPS) was employed to investigate the surface chemical compositions and the valence of elements. The high-resolution XPS spectra indicate Fe and Cu cations are mainly present as Fe³⁺ and Cu²⁺, respectively. The Cr 2p spectra suggest the existence of Cr³⁺ and Cr⁶⁺. The Co 2p and Ni 2p spectra show that there are the corresponding divalent and trivalent species (Figure S3). Notably, the O 1s core level spectra can be deconvoluted into three peaks at 529.8, 531.4, and 532.8 eV, corresponding to oxygen atoms bound to metals (O1), defect sites with a low oxygen coordination (O2), and hydroxyl species or surface-adsorbed oxygen (O3), respectively (Figure 2 a).^[42] The much higher O2 ratio of P-HEOs indicates that P-HEOs possess higher concentration of oxygen vacancies than C-HEOs. Additionally, we used the electron paramagnetic resonance (EPR) spectroscopy to further identify the oxygen vacancies, which is an effective tool to detect unpaired electrons in materials.^[43] The P-HEOs showcase an obviously stronger EPR signal at $g = 2.003$ (Figure 2 b). The signal intensity illustrates P-HEOs have more oxygen vacancies that is in good agreement with the XPS results. It is anticipated that oxygen vacancies engineering provides a promising opportunity to regulate the electronic structures of oxides to effectively boost the electrocatalytic activity.^[18,44,45]

Our method can synthesize a series of HEOs at low-temperature, illustrating the reliability and generality of the plasma strategy. As expected, XRD patterns of the synthesized HEOs reveal that the diffraction peaks are indexed to the single-phase spinel structure (Figure S4). TEM images confirm a typical nanosheets structure with the sizes from about 20 to 100 nm (Figure S5). The elemental mappings suggest the homogeneous dispersion of each element within these HEOs nanosheets without phase separation (Figures 3 a–f), consistent with the results of EDX and ICP-OES (Figure S6, Table S1 and S2). XPS spectra further confirm different HEOs contain corresponding metal and oxygen elements, and O 1s spectra disclose these HEOs possess rich oxygen vacancies (Figures S7–12). All these results demonstrate that our method is able to extend to more complex

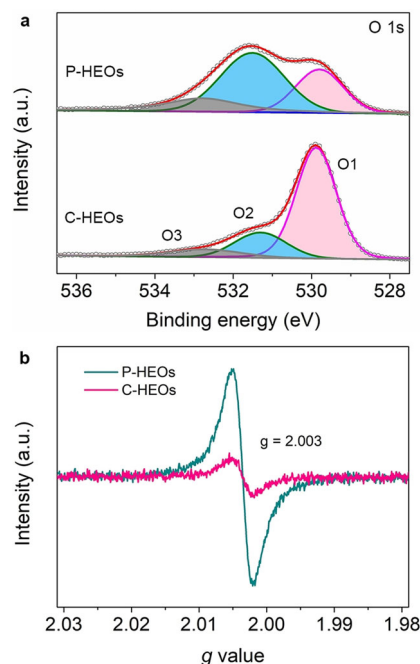


Figure 2. a) O 1s XPS and b) EPR spectra of P-HEOs and C-HEOs.

HEOs nanosheets with abundant oxygen vacancies (defects) by tailoring the elemental composition.

As a proof of concept, we applied the P-HEOs nanosheets loaded on glassy carbon electrode for HMF oxidation. The P-HEOs exhibit the onset potential of 1.50 V vs. RHE for the OER (Figure S13). After introducing HMF, the P-HEOs electrode shows higher current response, and the onset potential decrease to 1.35 V vs. RHE, which is much lower than that of C-HEOs (Figure 4 a), implying the excellent electrocatalytic activity on the P-HEOs electrode. Furthermore, the electrocatalytic activity of P-HEOs is superior to that of oxides with fewer elements (Figure S14). The Tafel slope of P-HEOs and C-HEOs is calculated to be 97.8 and 279.5 mV dec⁻¹, respectively (Figure 4 b). The smaller slope of P-HEOs indicates significantly improved kinetics towards HMF electrooxidation. Electrochemically active surface area (ECSA) was evaluated by double-layer capacitance (C_{dl}). The C_{dl} of P-HEOs (1.22 mF cm⁻²) is higher than that of C-HEOs (0.34 mF cm⁻²) (Figure S15), suggesting the nanosheets structure of P-HEOs could increase the ECSA and expose more active sites. The current density normalized by ECSA and BET at 1.50 V vs. RHE of P-HEOs is about 7-fold and 2-fold higher than that of C-HEOs (Figure 4 c and S16), verifying the surface abundant oxygen vacancies can enhance the intrinsic activity of P-HEOs.^[30]

Electrochemical impedance spectroscopy (EIS) was used to probe the interfacial electrochemical behavior between electrode and electrolyte. The equivalent circuit and the parameters of each component were presented by fitting the Nyquist plots (Figure S17 and Table S3). It is evident that the R_{ct} of P-HEOs (113.9 Ω) is smaller than that of C-HEOs (396.5 Ω), demonstrating P-HEOs has faster charge transfer rate (Figure 4 d). Furthermore, in situ EIS at various potentials was used to investigate the charge-transfer resistance

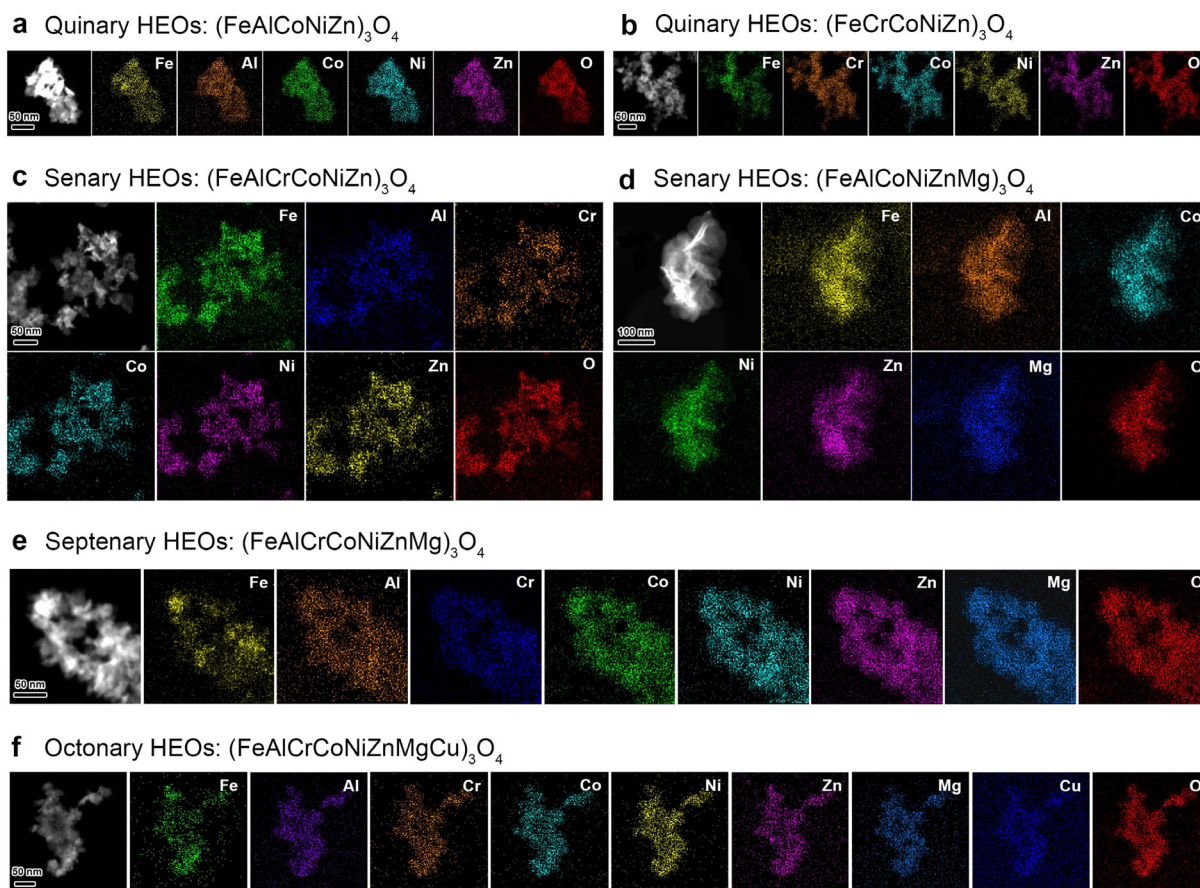


Figure 3. EDX elemental mapping of HEOs: a) $(\text{FeAlCoNiZn})_3\text{O}_4$, b) $(\text{FeCrCoNiZn})_3\text{O}_4$, c) $(\text{FeAlCrCoNiZn})_3\text{O}_4$, d) $(\text{FeAlCoNiZnMg})_3\text{O}_4$, e) $(\text{FeAlCrCoNiZnMg})_3\text{O}_4$, and f) $(\text{FeAlCrCoNiZnMgCu})_3\text{O}_4$.

change and catalytic kinetics of P-HEOs electrode during HMF oxidation processes. At the low potential of 1.05–1.30 V vs. RHE, Nyquist plots show steep straight lines, which indicate the infinite charge-transfer resistance. When the applied potential exceeds 1.35 V, an apparent semicircle appears, which indicates the HMF electro-oxidation has occurred (Figure 4e). The Bode phase plots depict the trend of phase angle variation with frequency. Generally, the peaks in low frequency and high frequency region are regarded as the interface reaction charge transfer and the electron transfer process associated with the formation of surface oxidative species, respectively.^[46,47] As shown in Figure 4f, when the potential window is 1.35–1.55 V, the decreasing of peak at low frequency, corresponding to the accelerating of interface reaction charge transfer, indicates the faster kinetics of HMF electrooxidation. In high frequency, the peak position regularly shifts to higher frequency with potential from 1.35 to 1.55 V, mainly attributed to the accelerating of surface metal oxidation, which is closely related to the increasing of HMF oxidation current.

To realize high current density and conversion efficiency, the P-HEOs were dispersed onto carbon paper as the electrode for HMF oxidation. P-HEOs yield a higher current density and a lower onset potential than C-HEOs (Figure S18). The chronoamperometric tests were carried out at 1.50 V vs. RHE and the concentration of HMF and its

oxidation products with the reaction progressed was calculated by HPLC quantitatively (Figures 4g and S19). As depicted in Figure 4h, the concentration of HMF decreased and the level of FDCA increased with the increasing charge, indicating the successful conversion of HMF to FDCA. Note that the concentration of 2,5-diformylfuran (DFF) is almost absent, while the concentration changes of 5-hydroxymethyl-2-furancarboxylic acid (HMFA) and 2-formyl-5-furancarboxylic acid (FFCA) were detectable, suggesting FDCA is likely generated following the route of HMFA intermediate (Figure S20). In six successive electrolysis cycles, no obvious decay was observed in FDCA yield and Faradaic efficiency (Figure 4i), strongly highlighting the cycling durability of the P-HEOs electrode. The P-HEOs after stability tests were investigated by TEM, EDX, and XPS, and the results corroborate that there are no obvious changes in architecture, composition, and structure (Figure S21 and S22). This high stability results from favorable high-entropy effect. We finally investigated the electrocatalytic performance of P-HEOs for other substrates, such as ethanol, benzyl alcohol, furfuryl alcohol, furfural, glycerol, and glucose. The P-HEOs electrode exhibits low onset potential and rapid current rise (Figure S23), manifesting the P-HEOs nanosheets has the potential for electrochemical biomass conversion.

In summary, we have successfully developed a versatile and efficient strategy for the synthesis of nanostructured

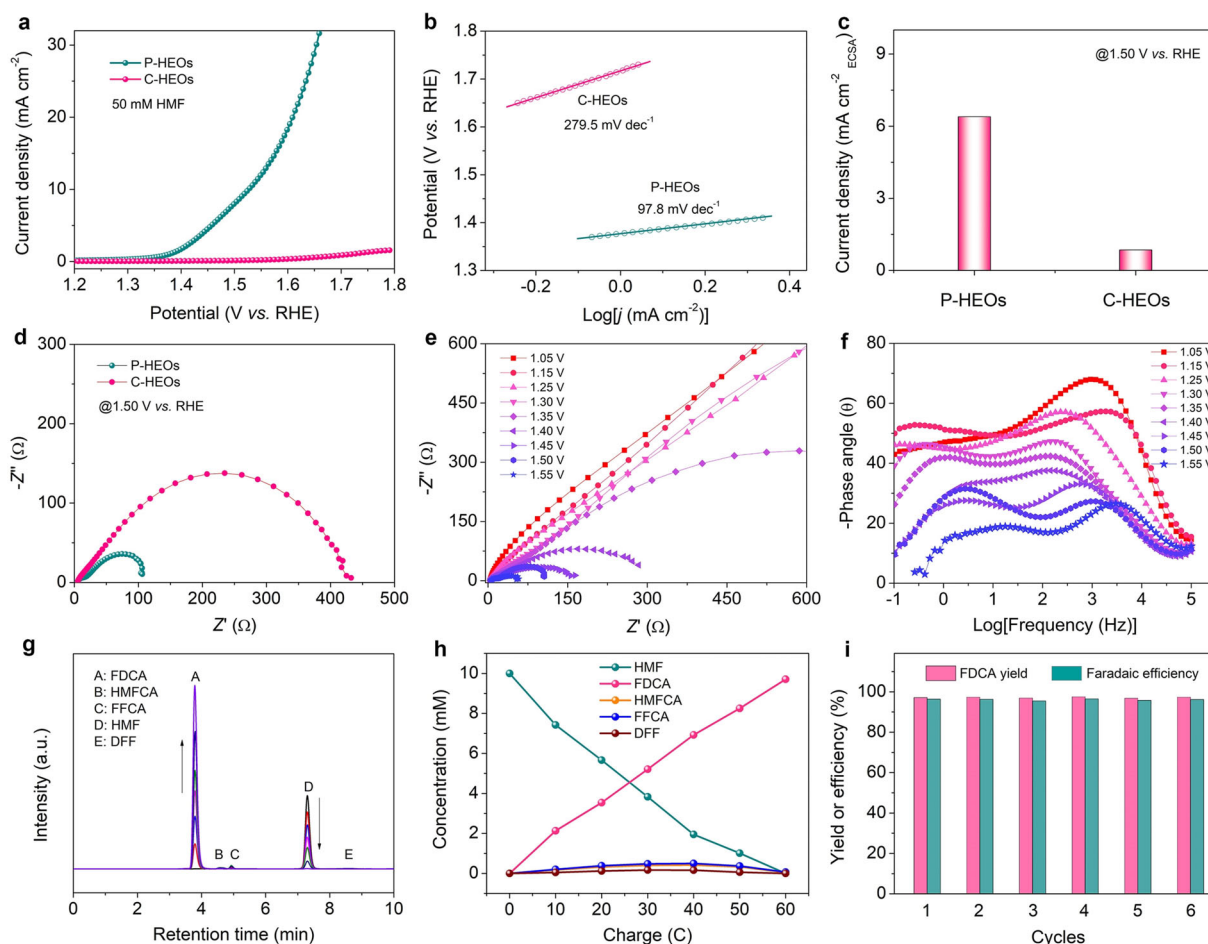


Figure 4. a) LSV curves and b) Tafel plots of P-HEOs and C-HEOs in 1.0 M KOH with 50 mM HMF. c) Current density normalized by ECSA at 1.50 V vs. RHE. d) Nyquist plots at 1.50 V vs. RHE. e) Nyquist and f) Bode phase plots of P-HEOs at various voltages vs. RHE. g) HPLC traces of HMF oxidation catalyzed by P-HEOs at 1.50 V vs. RHE in 1.0 M KOH with 10 mM HMF. h) Concentration changes of HMF and its oxidation products during HMF electrooxidation. i) FDCA yield and Faradaic efficiency of P-HEOs under six successive cycles.

HEOs at low-temperature. The proposed plasma strategy ensures the nanosheets structure, abundant surface oxygen vacancies, and high surface area of the obtained HEOs, efficiently promoting the electrocatalytic activity. As a proof of concept, the quinary HEOs nanosheets exhibit superior electrocatalytic performance for HMF oxidation with lower onset potential and faster kinetics, providing a promising platform for efficient electrochemical biomass upgrading.

Acknowledgements

This work was supported by the national key R&D program of china 2020YFA0710000, the National Natural Science Foundation of China (Grant Nos. 21701043, 22002039, 21825201 and U19A2017), the Provincial Natural Science Foundation of Hunan (2019GK2031), the China Postdoctoral Science Foundation (Grant Nos. 2020M682549, 2020M682541, 2020M682542, and 2020M672473), the Science and Technology Innovation Program of Hunan Province, China (Grant Nos. 2020RC2020 and 2020RC2023), and

Changsha Municipal Natural Science Foundation (Grant No.: kq2007009).

Conflict of Interest

The authors declare no conflict of interest.

Keywords: biomass upgrading · defect chemistry · electrocatalysis · high-entropy oxides · plasma technology

- [1] S. A. Akhade, N. Singh, O. Y. Gutiérrez, J. Lopez-Ruiz, H. Wang, J. D. Holladay, Y. Liu, A. Karkamkar, R. S. Weber, A. B. Padmaperuma, M. Lee, G. A. Whyatt, M. Elliott, J. E. Holladay, J. L. Male, J. A. Lercher, R. Rousseau, V. Glezakou, *Chem. Rev.* **2020**, *120*, 11370–11419.
- [2] Q. Hou, X. Qi, M. Zhen, H. Qian, Y. Nie, C. Bai, S. Zhang, X. Bai, M. Ju, *Green Chem.* **2021**, *23*, 119–231.
- [3] J. Wang, J. Xi, Q. Xia, X. Liu, Y. Wang, *Sci. China Chem.* **2017**, *60*, 870–886.
- [4] H. G. Cha, K. Choi, *Nat. Chem.* **2015**, *7*, 328–333.
- [5] B. You, X. Liu, N. Jiang, Y. Sun, *J. Am. Chem. Soc.* **2016**, *138*, 13639–13646.

- [6] B. You, N. Jiang, X. Liu, Y. Sun, *Angew. Chem. Int. Ed.* **2016**, *55*, 9913–9917; *Angew. Chem.* **2016**, *128*, 10067–10071.
- [7] N. Zhang, Y. Zou, L. Tao, W. Chen, L. Zhou, Z. Liu, B. Zhou, G. Huang, H. Lin, S. Wang, *Angew. Chem. Int. Ed.* **2019**, *58*, 15895–15903; *Angew. Chem.* **2019**, *131*, 16042–16050.
- [8] X. Huang, J. Song, M. Hua, Z. Xie, S. Liu, T. Wu, G. Yang, B. Han, *Green Chem.* **2020**, *22*, 843–849.
- [9] G. Yang, Y. Jiao, H. Yan, Y. Xie, A. Wu, X. Dong, D. Guo, C. Tian, H. Fu, *Adv. Mater.* **2020**, *32*, 2000455.
- [10] W. Zhang, P. K. Liaw, Y. Zhang, *Sci. China Mater.* **2018**, *61*, 2–22.
- [11] C. Oses, C. Toher, S. Curtarolo, *Nat. Rev. Mater.* **2020**, *5*, 295–309.
- [12] Y. Yao, Z. Huang, P. Xie, S. D. Lacey, R. J. Jacob, H. Xie, F. Chen, A. Nie, T. Pu, M. Rehwoldt, D. Yu, M. R. Zachariah, C. Wang, R. Shahbazian-Yassar, J. Li, L. Hu, *Science* **2018**, *359*, 1489.
- [13] T. Jin, X. Sang, R. R. Unocic, R. T. Kinch, X. Liu, J. Hu, H. Liu, S. Dai, *Adv. Mater.* **2018**, *30*, 1707512.
- [14] C. M. Rost, E. Sachet, T. Borman, A. Moballegh, E. C. Dickey, D. Hou, J. L. Jones, S. Curtarolo, J. Maria, *Nat. Commun.* **2015**, *6*, 8485.
- [15] A. Sarkar, Q. Wang, A. Schiele, M. R. Chellali, S. S. Bhattacharya, D. Wang, T. Brezesinski, H. Hahn, L. Velasco, B. Breitung, *Adv. Mater.* **2019**, *31*, 1806236.
- [16] D. Bérardan, S. Franger, D. Dragoe, A. K. Meena, N. Dragoe, *Phys. Status Solidi RRL* **2016**, *10*, 328–333.
- [17] T. Wang, H. Chen, Z. Yang, J. Liang, S. Dai, *J. Am. Chem. Soc.* **2020**, *142*, 4550–4554.
- [18] H. Xu, Z. Zhang, J. Liu, C. Do-Thanh, H. Chen, S. Xu, Q. Lin, Y. Jiao, J. Wang, Y. Wang, Y. Chen, S. Dai, *Nat. Commun.* **2020**, *11*, 3908.
- [19] D. Wang, Z. Liu, S. Du, Y. Zhang, H. Li, Z. Xiao, W. Chen, R. Chen, Y. Wang, Y. Zou, S. Wang, *J. Mater. Chem. A* **2019**, *7*, 24211–24216.
- [20] A. Sarkar, L. Velasco, D. Wang, Q. Wang, G. Talasila, L. de Biasi, C. Kübel, T. Brezesinski, S. S. Bhattacharya, H. Hahn, B. Breitung, *Nat. Commun.* **2018**, *9*, 3400.
- [21] C. Li, X. Han, F. Cheng, Y. Hu, C. Chen, J. Chen, *Nat. Commun.* **2015**, *6*, 7345.
- [22] J. Dąbrowa, M. Stygar, A. Mikula, A. Knapik, K. Mroczka, W. Tejchman, M. Danielewski, M. Martin, *Mater. Lett.* **2018**, *216*, 32–36.
- [23] C. Zhao, F. Ding, Y. Lu, L. Chen, Y. Hu, *Angew. Chem. Int. Ed.* **2020**, *59*, 264–269; *Angew. Chem.* **2020**, *132*, 270–275.
- [24] A. Sarkar, R. Djenadic, N. J. Usharani, K. P. Sanghvi, V. S. K. Chakravadhanula, A. S. Gandhi, H. Hahn, S. S. Bhattacharya, *J. Eur. Ceram. Soc.* **2017**, *37*, 747–754.
- [25] Z. W. Seh, J. Kibsgaard, C. F. Dickens, I. Chorkendorff, J. K. Nørskov, T. F. Jaramillo, *Science* **2017**, *355*, d4998.
- [26] X. Liu, J. Huang, Q. Zhang, L. Mai, *Adv. Mater.* **2017**, *29*, 1601759.
- [27] J. Feng, F. Lv, W. Zhang, P. Li, K. Wang, C. Yang, B. Wang, Y. Yang, J. Zhou, F. Lin, G. Wang, S. Guo, *Adv. Mater.* **2017**, *29*, 1703798.
- [28] W. Zhang, Z. Wu, H. Jiang, S. Yu, *J. Am. Chem. Soc.* **2014**, *136*, 14385–14388.
- [29] C. R. McCormick, R. E. Schaak, *J. Am. Chem. Soc.* **2021**, *143*, 1017–1023.
- [30] D. Yan, Y. Li, J. Huo, R. Chen, L. Dai, S. Wang, *Adv. Mater.* **2017**, *29*, 1606459.
- [31] F. Lei, Y. Sun, K. Liu, S. Gao, L. Liang, B. Pan, Y. Xie, *J. Am. Chem. Soc.* **2014**, *136*, 6826–6829.
- [32] X. Zhang, Y. Zhao, Y. Zhao, R. Shi, G. I. N. Waterhouse, T. Zhang, *Adv. Energy Mater.* **2019**, *9*, 1900881.
- [33] C. Hu, L. Zhang, L. Li, W. Zhu, W. Deng, H. Dong, Z. Zhao, J. Gong, *Sci. China Chem.* **2019**, *62*, 1030–1036.
- [34] Z. Geng, X. Kong, W. Chen, H. Su, Y. Liu, F. Cai, G. Wang, J. Zeng, *Angew. Chem. Int. Ed.* **2018**, *57*, 6054–6059; *Angew. Chem.* **2018**, *130*, 6162–6167.
- [35] S. Dou, L. Tao, R. Wang, S. El Hankari, R. Chen, S. Wang, *Adv. Mater.* **2018**, *30*, 1705850.
- [36] X. Wang, L. Zhuang, Y. Jia, H. Liu, X. Yan, L. Zhang, D. Yang, Z. Zhu, X. Yao, *Angew. Chem. Int. Ed.* **2018**, *57*, 16421–16425; *Angew. Chem.* **2018**, *130*, 16659–16663.
- [37] K. Gu, X. Zhu, D. Wang, N. Zhang, G. Huang, W. Li, P. Long, J. Tian, Y. Zou, Y. Wang, R. Chen, S. Wang, *J. Energy Chem.* **2021**, *60*, 121–126.
- [38] Y. Huang, S. L. Zhang, X. F. Lu, Z. Wu, D. Luan, X. W. D. Lou, *Angew. Chem. Int. Ed.* **2021**, *60*, 11841–11846; *Angew. Chem.* **2021**, *133*, 11947–11952.
- [39] J. Kibsgaard, Z. Chen, B. N. Reinecke, T. F. Jaramillo, *Nat. Mater.* **2012**, *11*, 963–969.
- [40] P. Chen, L. Wang, G. Wang, M. Gao, J. Ge, W. Yuan, Y. Shen, A. Xie, S. Yu, *Energy Environ. Sci.* **2014**, *7*, 4095–4103.
- [41] Y. Chen, C. Wang, Z. Wu, Y. Xiong, Q. Xu, S. Yu, H. Jiang, *Adv. Mater.* **2015**, *27*, 5010–5016.
- [42] J. Yin, J. Jin, M. Lu, B. Huang, H. Zhang, Y. Peng, P. Xi, C. Yan, *J. Am. Chem. Soc.* **2020**, *142*, 18378–18386.
- [43] Y. Bo, H. Wang, Y. Lin, T. Yang, R. Ye, Y. Li, C. Hu, P. Du, Y. Hu, Z. Liu, R. Long, C. Gao, B. Ye, L. Song, X. Wu, Y. Xiong, *Angew. Chem. Int. Ed.* **2021**, *60*, 16085–16092; *Angew. Chem.* **2021**, *133*, 16221–16228.
- [44] L. Zhuang, L. Ge, Y. Yang, M. Li, Y. Jia, X. Yao, Z. Zhu, *Adv. Mater.* **2017**, *29*, 1606793.
- [45] Y. Zhao, Y. Zhao, R. Shi, B. Wang, G. I. N. Waterhouse, L. Wu, C. Tung, T. Zhang, *Adv. Mater.* **2019**, *31*, 1806482.
- [46] R. L. Doyle, M. E. G. Lyons, *J. Electrochem. Soc.* **2013**, *160*, H142–H154.
- [47] C. Xie, W. Chen, S. Du, D. Yan, Y. Zhang, J. Chen, B. Liu, S. Wang, *Nano Energy* **2020**, *71*, 104653.

Manuscript received: June 2, 2021

Accepted manuscript online: June 25, 2021

Version of record online: ■■■■■■

Communications

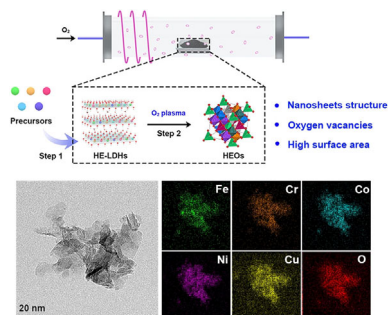


Electrocatalysis

K. Gu, D. Wang, C. Xie, T. Wang,
G. Huang, Y. Liu, Y. Zou,* L. Tao,*
S. Wang*



Defect-Rich High-Entropy Oxide
Nanosheets for Efficient 5-
Hydroxymethylfurfural Electrooxidation



Defect-rich high-entropy oxides (HEOs) nanosheets with high surface area are synthesized through a plasma strategy under low-temperature. The unique structural and compositional advantages endow the HEOs nanosheets with superior electrocatalytic activity for 5-hydroxymethylfurfural oxidation.